IEEE Access
Multidisciplinary | Rapid Review | Open Access Journal

Received February 1, 2022, accepted February 15, 2022, date of publication February 22, 2022, date of current version March 7, 2022.

Digital Object Identifier 10.1109/ACCESS.2022.3153505

Three-Phase Single-Stage Photovoltaic System With Synchronverter Control: Power System Simulation Studies

AJINKYA J. SONAWANE, (Graduate Student Member, IEEE), AND AMOD C. UMARIKAR, (Member, IEEE)

Discipline of Electrical Engineering, Indian Institute of Technology Indore, Indore 453552, India

Corresponding author: Ajinkya J. Sonawane (phd1501202009@iiti.ac.in)

This work was supported by the Department of Science and Technology (DST) Fund for Improvement of Science and Technology Infrastructure (FIST) Program under Grant SR/FST/ETI-400.

ABSTRACT The performance of a grid forming inverter integrating solar PV/Wind farms with the grid is currently a topic of wide interest. Synchronverter control is one of the well-known grid forming converter techniques. Evaluation of synchronverter control in the benchmark system will help in understanding its operation when connected to a larger system. Therefore, this article investigates the performance of three phase single-stage photovoltaic (PV) system with a synchronverter control in the North American medium voltage (MV) benchmark system. The main objective is to conduct an exploratory study of the PV based synchronverter system when subjected to various disturbances. The modeling of PV array, controllers like synchronverter, dc-link voltage control, ac voltage control and their design is discussed in detail. The simulation studies for different cases are carried out by creating various disturbances like changes in solar radiation, temperature, load, faults, etc., in the benchmark system. Furthermore, under fault conditions, response with/without voltage droop mechanism in synchronverter is studied. All the offline simulations are carried out in PSCAD/EMTDC environment. Further, the real time test studies are validated on Controller-Hardware-In-Loop (CHIL) platform in Real-Time-Digital-Simulator (RTDS). From this simulation study, it is concluded that Synchronverter Control can be a viable option when used as a grid forming technique.

INDEX TERMS Distribution generators, grid-connected inverter, PV-synchronverter system, synchronverter, virtual synchronous generators (VSG).

NOMENCLATURE

LIST OF ABBREVIATIONS

PV	Photovoltaic.
MV	Medium voltage.
CHIL	Controller-Hardware-In-Loop.
RTDS	Real-Time-Digital-Simulator.
STC	Standard Test Conditions.
DG	Distribution generator.
DPC	Direct power control.
EDPC	Enhanced direct power control.
DFIG	Doubly Fed Induction Generator.
WT	Wind Turbine.
VOC	Virtual oscillator control.
SPC	Synchronous power control.
VSG	Virtual Synchronous Generator.
VSC	Voltage source converter.
SG	Synchronous generator.
ES	Energy storage.
VSI	Voltage source inverter.
PCC	Point of common coupling.
IGBT	Insulated Gate Bipolar Transistors.
SPWM	Sinusoidal Pulse Width Modulation.
MPPT	Maximum power point tracking.
RoCoF	Rate of change of frequency.
DSP	Digital signal processor.

LIST OF SYMBOLS

V	Output voltage of PV cell [V].
I	Output current of PV cell [A].
V_{pv}	Output voltage across PV array [V].
I_{pv}	Output current of PV array [A].
R_{shpv}	Equivalent shunt resistance of PV cell [Ω].
R_{spv}	Equivalent series resistance of PV cell [Ω].
I_{phx}	Photocurrent of each PV cell [A].
I_{ox}	Reverse saturation current [A].

The associate editor coordinating the review of this manuscript and approving it for publication was Yuh-Shyan Hwang.

$I_{sc(STC)}$	Panel short circuit current at STC [A].
$V_{oc(STC)}$	Open circuit voltage of a PV panel at STC [V].
n_s	Number of cells in series per panel.
n_p	Number of cells in parallel per panel.
N_s	Number of panels in series.
N_p	Number of panels in parallel.
T_s	Standard temperature at STC [^{o}K].
T	Operating temperature of the PV panel [^{o}K].
K_i	Temperature coefficient of PV short circuit current [$\%/^oC$].
K_V	Temperature coefficient of PV open circuit voltage [$\%/^oC$].
G_{nom}	Nominal solar radiation at STC [W/m^2].
G	Solar radiation at STC [W/m^2].
q	Charge of electron 1.602×10^{-19} [C].
k	Boltzmann's constant 1.38064×10^{-23} [J/K].
n	Ideality factor.
V_{dc}	Dc-link voltage [V].
I_{dc}	Dc input current to the VSC [A].
C_{dc}	Dc-link capacitance [μf].
m	Modulation index.
m_d	d-axis modulation index.
m_q	q-axis modulation index.
i_{sd}	d-axis output current of VSC [A].
i_{sq}	q-axisoutput current of VSC [A].
L_f	Inductance of filter [mH].
R_f	Internal resistance of L_f [Ω].
C_f	Filter capacitor [μf].
R_d	Damping resistance in series with C_f [Ω].
L_t	Leakage inductance of the interface transformer [mH].
P_{pv}	Output power of PV array [W].
P_s	Output power of the inverter [W].
P_{cdc}	Power stored in a dc-link capacitor [W].
V_{pcc}	Voltage amplitude of PCC voltage [V].

I. INTRODUCTION

Distribution generators (DGs) are gaining popularity due to its technical and environmental benefits and become an alternative solution to solve the energy crisis[1].Power electronic converters are used in DGs to interface with the grid to improve the performance of DGs and ensure power quality. The increase in penetration of DGs has challenged the grid network in terms of intermittent power generation, fault current level, etc. Large disturbance in the system is caused by voltage spikes and inrush current, which may damage power electronic devices [2]–[4]. These large disturbances pose significant challenges for the stable operation of DGs. This concern has motivated the application of power electronic converters to support the grid and allows more renewable energy to integrate with the grid.

Traditionally, the power converters are operating in a grid following mode and act as a current source with conventional current control techniques [5]. In [6], the PV-based grid-connected inverter simulation study is carried out with conventional current control technique. The study is carried on MV benchmark system, which includes a principle of operation, parameter selection, control design and fault analysis of system. Apart from the grid following converters, grid forming converters are now coming into picture. Different grid forming controller strategies are discussed in [7]–[12]. Droop control grid forming techniqueoriginates from the governor action and enables sharing the power as per VSCs rating when operating in parallel. The stability issues are arise in droop control when high droop gain is used [8]. Another grid forming approach is direct power control (DPC), in which output voltage gives the phase angle reference and that is why it is categorized in a grid forming converter [9]–[10]. The enhanced direct power control (EDPC) is proposed in [11], for Doubly Fed Induction Generator (DFIG) driven by variable speed Wind Turbine (WT) application. In this approach, the switching pattern for VSCs is produced from hysteresis control. The virtual oscillator control (VOC) is coupled oscillator-based grid forming control. The key advantage of VOC is that it synchronizes the parallel connected inverter without inter-inverter communication [8]. The swing equation-based control with virtual inertia capabilities based synchronous power control (SPC) is another grid forming control approach [12]. It has a cascaded control structure with inner current control, outer voltage control and reference for outer control is generated by the swing equation. Hence, it creates complexity in tunning of controller [12]. 'Virtual Synchronous Generator' (VSG) is one of the techniques used in grid forming converters that emulates inertia [13]–[16]. The idea is to make a voltage source converter (VSC) work like a synchronous generator (SG). Synchronverter is one of the various models of VSG [17] and operates the power converters in grid forming mode by implementing self-synchronize technique [18]. The mathematical equation and control part which regulates the frequency and voltage of SG are embedded in the controller so that it mimics SG and extracts several advantages of it. The core advantage of the synchronverter is that it provides inertia for frequency regulation. For the realization of inertia support, VSG control applied to VSC requires energy storage (ES) such as dc-link capacitor, supercapacitor and batteries [19]. There are several studies present in the literature that discusses various aspects of synchronverters like stability analysis and dynamic performance, active and reactive power loop decoupling, small-signal modeling, modified synchronverter, etc. [20]–[23]. One of the major challenges in system is coping with various types of faults, which damages the power electronics devices. Fault analysis study of the synchronverter is done in [24]. It does asymmetric fault analysis using the instantaneous symmetric component method. It can be noted that in the literature, fault analysis of synchronverter based system always considers source as an ideal dc source. To the best of the authors knowledge, fault analysis with PV source is yet to be carried out.

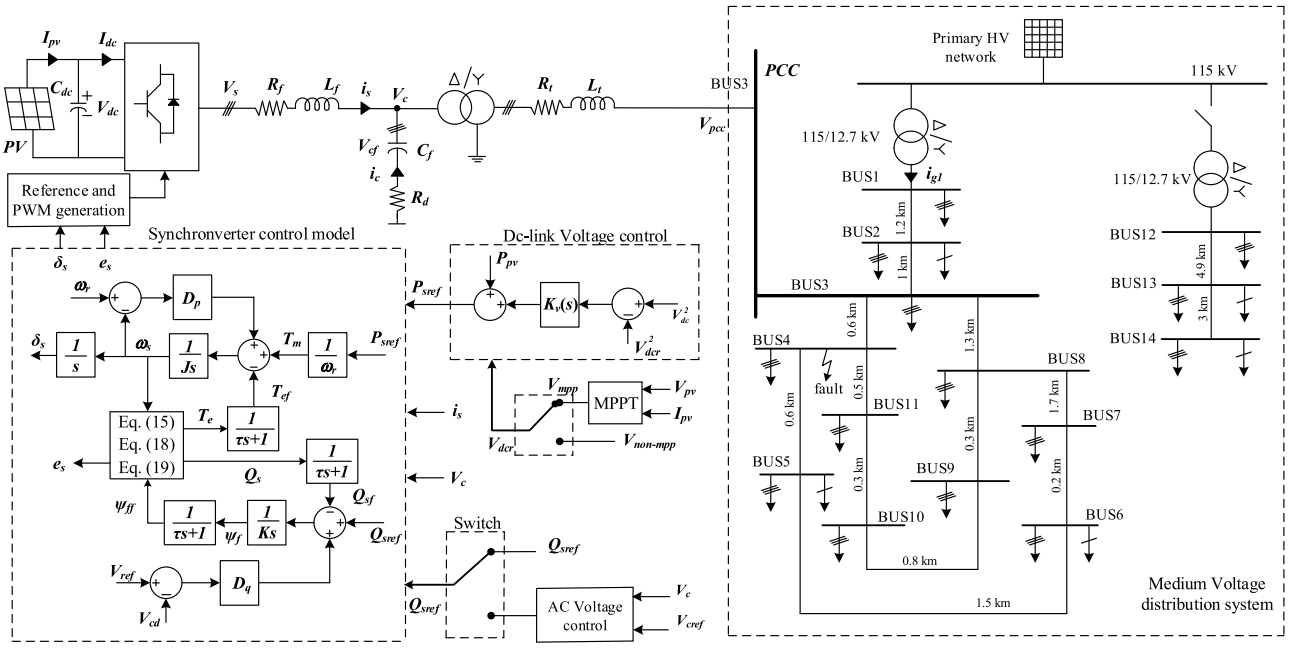

FIGURE 1. Diagram of PV-based synchronverter VSC system connected to MV distribution system.

Commonly, PV systems are connected to the power system at sub transmission voltage level. PV systems are anticipated to be connected to distribution networks where loads and local generators are also present. For better understanding of control, dynamic characteristics, and performance of large scale PV systems to be employed as DGs, a detailed study on benchmark system is required. A similar study is performed on 1.4 MW PV system in [6] with the conventional current control in grid following mode. On the same line, and in view of the ongoing development in grid forming converters, a similar study is required to be performed on the synchronverter, which is one of the grid forming technique. From the literature, it is apparent that such a performance investigation of synchronverter on a benchmark system considering a PV source is yet to be carried out.

This article investigates the performance of the PV synchronverter on benchmark system, which is North American Medium Voltage distribution system [25]. The contributions can be summarized as follows:

- Modeling of the power circuit, the control scheme and controller design of the grid connected PV system is presented to help in developing a synchronverter control based grid forming simulation model for study.
- Response of the system with the change in parameters like change in solar radiation, change in load, control parameter J is explored.
- Response of PV system with MPP and nonMPP mode of operation is studied when a disturbance is created in the distribution system.
- Effect of disturbance created in distribution system on voltage profile and voltage regulation is studied.
- Also, performance of the PV system for different fault conditions is investigated and the contribution of voltage droop mechanism is highlighted.
- The system under study is simulated using PSCAD/EMTDC software. It is validated through CHIL real time simulation using RTDS.

The organization of the paper is as follows. Section II describes the details of the power circuit. Section III discusses the controller in PV system. Section IV describes the controllers design. Section V discusses simulation of the system under various conditions. Section VI shows Real Time Simulation results with CHIL and RTDS. Possible future extensions of the present work are discussed in section VII. Section VIII presents the conclusion.

II. PV-SYNCHRONVERTER WITH NORTH AMERICAN MV BENCHMARK SYSTEM

Fig. 1 shows the complete system taken for study. PV source rating is taken as 1.4 MW which is achieved by a combination of series and parallel PV panels called PV array. The PV panels generate the low voltage; hence PV array is formed to build higher voltage for single-stage configuration, which is around 800 V at maximum power point (MPP) and around 1000 V at open circuit. The dc-link capacitor C_{dc} is connected parallel to the PV array to maintain the dc-link voltage V_{dc}. The single-stage IGBT based voltage source inverter (VSI) is used as an interface between the PV source and distribution system. The output of VSI is interfaced with the grid at point of common coupling (PCC), using a low pass filter and interface transformer. The high-frequency harmonics injected by PV system into the grid are filtered

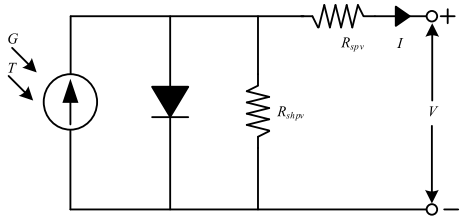

FIGURE 2. Equivalent circuit of single diode PV cell.

using LCL filter. L_f is a filter inductor in series with resistance R_f. R_f represents the internal resistance of inductor L_f and resistance of IGBT switches. C_f is a filter capacitor in series with damping resistance R_d. Current through inductor L_f, voltage across capacitor C_f and voltage across dc-link capacitor C_{dc} and PV current I_{pv} are used as feedback signals for the controller. The VSI is connected to the benchmark system through Δ/Y interface transformer. The leakage inductance of the interface transformer is represented as L_t. The PV system is connected to the North American MV network, which is addressed by CIGRE Task Force [25]. This benchmark system is for network integration of DGs and this test system facilitates the analysis and validation of developed methods and techniques [26]. The primary HV voltage is 115 kV and then it is step down to 12.47 kV. The network lines are modeled as PI model and network loads are modeled as voltage dependent loads. On each bus, loads are connected, and some buses also have single phase subnetwork. The benchmark system has unbalance distribution of load. The PV system is connected to benchmark system at BUS 3, as shown in Fig. 1. Some of the simulation case studies are carried out by creating a disturbance in the distribution system. The tests are carried out by creating fault on bus 4 as shown in Fig. 1, or disconnecting load on bus 1, as the maximum load is connected on bus 1.

A. PV POWER GENERATION

The low power PV cells are connected in large units to form a PV module. PV modules are connected in series and parallel to form a PV panel. The combination of series and parallel connection of PV panel constitutes a PV array. The entire PV generation is also called as a PV farm. The different equivalent circuits of PV cells have been proposed in literature [27]–[29], for example, single-diode, two-diodes and three-diodes equivalent circuits of PV cell. The single diode based PV cell circuit is widely used for power system studied because of its simplicity and accuracy [30]. The equivalent circuit of single diode PV cell is shown in Fig.2. It consists of a diode connected in parallel with current source, parallel resistance R_{shpv} representing the leakage resistance of *pn* junction and series resistance R_{spv} represents the internal resistance of PV cell.

In this article, a PV cell model is based on an equivalent single diode circuit, which is proposed in [30]. The required capacity of PV power system is generated by connecting PV

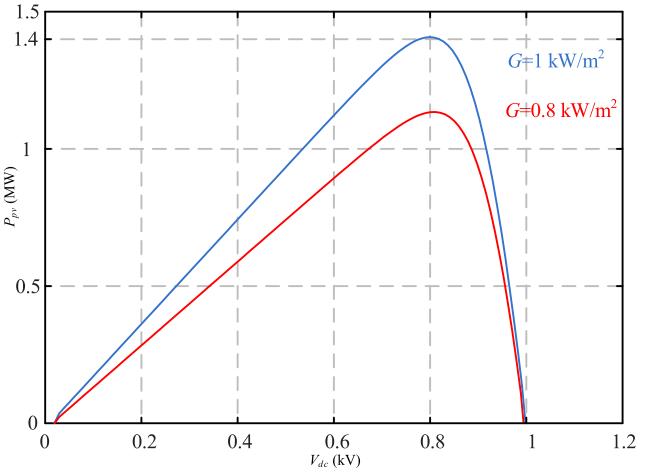

FIGURE 3. PV curve of simulated PV model.

panels in series and parallel to create complete PV panel array. The mathematical model used to describe solar PV source is as follows [30], [31].

$$I_{pv} = a_1 G - a_2\{e^{a_3 V_{pv} + a_4 I_{pv}} - 1\} - a_5 V_{pv} \tag{1}$$

where, I_{pv} is a PV array current and voltage across PV panel is V_{pv}, which is equal to dc-link voltage V_{dc}. The coefficient of PV array a_1, a_2, a_3, a_4 and a_5 are derived from equation in [31].
Where,

$$a_1 = \frac{N_p I_{phx}}{K_1}, \quad a_2 = \frac{N_p I_{ox}}{K_1}, \; a_3 = \frac{q}{nkTn_s N_s}$$
$$a_4 = \frac{qR_{spv}}{nkTn_s N_s}, \quad a_5 = \frac{n_p N_p}{N_s n_s R_{shpv} K_1}, \; K_1 = \frac{R_{spv}}{R_{shpv}}$$

where, I_{phx} and I_{ox} are given in (2) and (3), as shown at the bottom of the next page, respectively. $I_{sc(STC)}$ is the panel short circuit current at Standard Test Conditions (STC), $V_{oc(STC)}$ is the open circuit voltage of a PV panel at STC. n_s and n_p are the number of cells in series per panel, and the number of cells in parallel per panel, respectively. N_s and N_p are the number of panels in series and the number of panel series strings in parallel, respectively. T_s is the standard temperature at STC and T is the operating temperature of the PV panel, R_{shpv} and R_{spv} are the equivalent shunt resistance and series resistance of each cell, K_i is temperature coefficient of PV short circuit current, K_V is temperature coefficient of PV open circuit voltage, G_{nom} is the solar radiation at STC, q is charge of electron and k is the Boltzmann's constant.

The PV curve of simulated PV model is shown in Fig. 3. The PV curve is simulated when maximum solar irradiance is available i.e., $G = 1$ kW/m^2 and for $G = 0.8$ kW/m^2. It is observed that the peak power is generated at 0.8 kV.

B. UTILITY INTERFACE

The PV power is injected into the grid by using dc-ac converter. The two-level inverter has two valves in each leg

and hence it consists of 6 Insulated Gate Bipolar Transistors (IGBT). The switching strategy used is Sinusoidal Pulse Width Modulation (SPWM). The relation between dc voltage and VSC output AC phase voltage magnitude of the fundamental component is given in (4).

$$V_s = \frac{V_{dc}}{2} m \tag{4}$$

where, V_s is AC output voltage of VSC in space phasor domain, m is a modulation index in space phasor domain and V_{dc} is a dc-link voltage input to VSC. The equation for dc-link voltage V_{dc} is given as:

$$\frac{dV_{dc}}{dt} = \frac{I_{pv}}{C_{dc}} - \frac{I_{dc}}{C_{dc}} \tag{5}$$

where, I_{dc} is a dc input current to the VSC and C_{dc} is dc-link capacitance. The input dc current is given as:

$$I_{dc} = \frac{3(m_d i_{sd} + m_q i_{sq})}{4} \tag{6}$$

where, m_d and m_q are modulation index in dq frame and i_{sd} and i_{sq} are output current of VSC in dq frame [32].

In the power system, inertia is provided by kinetic energy stored in a rotor of synchronous generator. The inertia coefficient of a synchronous generator is given as:

$$H = \frac{J\omega^2}{2VA_{rated}} \tag{7}$$

In the synchronous machine-based controller, the inertia is emulated by energy storage. In this paper, the inertia is provided by dc-link capacitor [33]. The inertia provided by dc-link capacitor is expressed as:

$$H = \frac{C_{dc}V_{dc}^2}{2VA_{rated}} \tag{8}$$

The close mapping between inertia coefficient equations of generator and dc-link capacitor is observed and clearly identified from equation (7) and (8). The ω and J plays a similar role as V_{dc} and C_{dc}, respectively. The detailed derivation for calculating equivalent inertia coefficient of the converter is given in [33].

The VSI is used for converting DC solar power to AC, which causes harmonics in output voltage and current due to switching frequency [32]. VSI frequency is generally chosen from 2 kHz to 15 kHz. These harmonics not only disturb the voltage and current but also disturb the equipment's. If same voltage and current are directly fed to the grid, it will distort the PCC voltage and current. To overcome this issue, the filter circuit is connected between VSI and grid, removing harmonics and injecting a nearly fundamental wave into the grid. The filter parameters are determined as a tradeoff between the harmonics injection and operation range of the controller. The most common filters for grid-connected application of the VSI are LC and LCL filters [34]. LC filter is a second order filter, whereas LCL filter is a third order filter. In comparison with LC filter, LCL filter has better performance in removing the harmonics. However, due to more poles and zeroes, the LCL filter makes the control plant more complicated [35]. To mitigate the resonance problem of LC and LCL filters, a resistor is connected in series with a filter capacitor [36]. Fig.1. shows the LCL filter for grid-connected VSI. In the modeling R_f represents the sum of IGBT on-state resistance and internal resistance of filter inductors L_f. The coupling transformer is modeled as an ideal transformer in series with leakage inductance L_t.

Filter parameters are determined based on several factors such as the harmonics of output current, the resonance frequency of LCL filter, voltage drop of filter inductance and reactive power compensation provided by the filter capacitor. Generally, to limit the VSI current ripple, the reactance of the filter inductor is selected between 0.1 to 0.25 pu [6]. The typical value of the current ripple is 10%-20% of the inverter current peak [37]. The voltage drop across the filter inductor can limit the voltage control by the VSI. Therefore, the voltage drop across the filter inductor should not exceed 0.3 pu. Otherwise, a higher dc-link voltage is needed to produce a specific AC voltage. Also, the amount of reactive power generated by the filter capacitor influences the reactive power compensation by the VSI. Hence, the filter capacitor value is designed to limit the reactive power exchange below 0.05 pu of the inverter power rate [37]. To avoid resonance between filter capacitor and inductor, a damping resistor is added to filter capacitor in series [36].

The values of filter inductance L_f and filter capacitance Cf are designed based on the following criteria:

1) The total harmonic distortion (THD) of voltage and current injected into the distribution network should be less than 5% [38].
2) In order to improve the ability of current for tracking and the speed of system response, L_f should be small, but a better filter effect is achieved if L_f is large. Hence a suitable value of L_f should be chosen considering these factors. The value of inductance is chosen such that the ripple of the output current is not more than

$$I_{phx} = \frac{[n_s I_{sc(STC)}(1 + K_i(T - T_s))(R_{shpv} + R_{spv}) - n_p V_{oc}][e^{\frac{qV_{oc(STC)}(1+K_V(T-T_s))}{nkTn_s}} - 1]}{n_s R_{shpv}[e^{\frac{qV_{oc(STC)}(1+K_V(T-T_s))}{nkTn_s}} - e^{\frac{qI_{sc(STC)}(1+K_i(T-T_s)R_{spv})}{nkTn_p}} G_{nom}]} + \frac{n_p V_{oc(STC)}(1 + K_V(T - T_s))}{n_s R_{shpv} G_{nom}} \tag{2}$$

$$I_{ox} = \frac{[n_s I_{sc(STC)}(1 + K_i(T - T_s))(R_{shpv} + R_{spv}) - n_p V_{oc}]}{n_s R_{shpv}[e^{\frac{qV_{oc(STC)}(1+K_V(T-T_s))}{nkTn_s}} - e^{\frac{qI_{sc(STC)}(1+K_i(T-T_s)R_{spv})}{nkTn_p}}]} \tag{3}$$

10% to 20% [37]. The following equation governs this:

$$\frac{V_{dc}}{4\sqrt{3}i_{ripple}f_{sw}} \leq L_f \leq \frac{\sqrt{\frac{V_{dc}^2}{3} - V_m^2}}{\omega I_m} \tag{9}$$

where, V_m is peak phase voltage, I_m is peak current, f_{sw} is switching frequency and i_{ripple} is a current ripple.

3) To avoid the lower power factor; generally, the reactive power absorbed from the capacitor filter C_f should be less than 5% of the nominal power of the system [37].

$$C_f \leq L_f \leq \frac{0.05Q_n}{3\omega V_m^2} \tag{10}$$

where, Q_n in rated reactive power of inverter and V_m is a peak value of phase voltage.

4) The resonant frequency of the LCL filter should be in the range between 10 times the line frequency and one half the switching frequency of VSC [37].

$$10\, f_o \geq f_{res} \geq 0.5 f_{sw} \tag{11}$$

where, f_o is a system frequency and f_{res} is resonance frequency. The resonance frequency can be obtained as:

$$f_{res} = \frac{1}{2\pi}\frac{L_f + L_t}{L_f L_t C_f} \tag{12}$$

A proper resistance R_d should be added in series with filter capacitor, such that there is sufficient damping of the resonant peak at the resonant frequency.

A coupling transformer brings the VSI output ac voltage to the PCC voltage level. Generally, it is a step-up transformer. The low voltage winding is Δ connected to avoid voltage disturbance due to the triple-n harmonics and high voltage winding is grounded star connected.

III. CONTROLLERS FOR PV SYSTEM

The overall control scheme consists of four different controllers like 1) synchronverter control, 2) dc-link voltage control, 3) ac voltage control, and 4) maximum power point tracking (MPPT). The controller schemes are discussed in the following subsection.

A. SYNCHRONVERTER CONTROL

Synchronverter emulates the characteristics of a synchronous generator (SG) and hence its response to disturbance is same as SG [17]. It mimics its mathematical equation to control active and reactive power by providing virtual inertia. Fig. 4 shows the synchronverter controller block diagram, which can be broadly divided into two parts, namely 1) Active power loop and 2) Reactive power loop.

1) ACTIVE POWER LOOP

When the disturbance occurs, synchronverter maintains the stability of system by controlling angular frequency of reference voltage by providing virtual inertia. The active power loop regulates the angular frequency ω_s and power angle

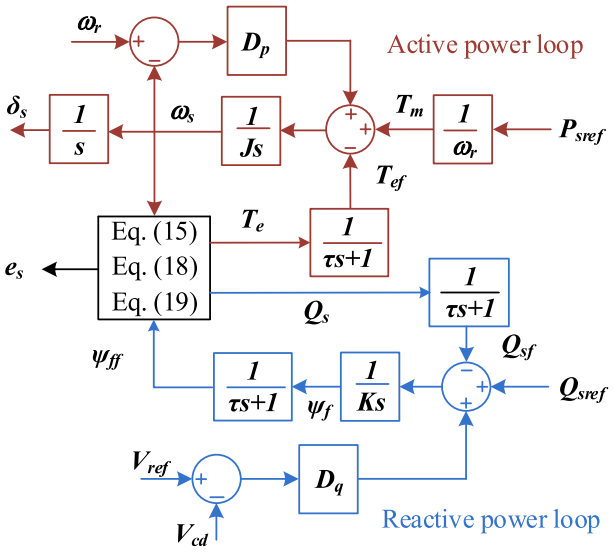

FIGURE 4. Control diagram of synchronverter control highlighting active and reactive power loop.

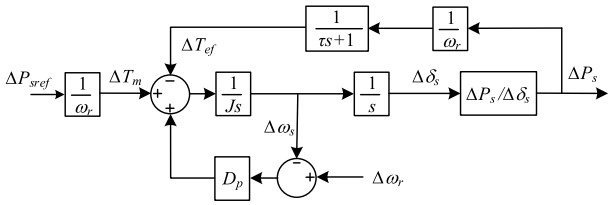

FIGURE 5. Small Signal model of an active power loop.

δ_s and this is done by emulating the swing equation given in (13).

$$\frac{d\omega_s}{dt} = \frac{1}{J}(T_m - T_{ef} + D_p(\omega_r - \omega_s)) \tag{13}$$

$$\frac{d\delta_s}{dt} = \omega_s \tag{14}$$

where J is inertia constant. T_m and T_e are mechanical and electrical torque, respectively; D_p is a damping coefficient. ω_s is a virtual speed of a synchronverter. ω_r is a reference value for ω_s. T_{ef} is a filtered output of T_e. The mechanical torque is computed as $T_m = P_{sref}/\omega_r$ where P_{sref} is the reference active power. The electrical torque is then evaluated as:

$$T_e = 1.5\psi_{ff} i_{sd} \tag{15}$$

The ψ_{ff} is the filtered output of excitation flux ψ_f, which is obtained from the synchronverter reactive power loop.

For controller design purposes, the small-signal model of the active power loop is shown in Fig. 5. $\Delta P_s/\Delta\delta_s$ is the small-signal change in active power to change in angle and expression for $\Delta P_s/\Delta\delta_s$ is given in the appendix. From Fig. 5, the transfer function $G_p(s)$ is given as:

$$G_p(s) = \frac{\Delta P_s}{\Delta P_{sref}} = \frac{(\tau s + 1)(\Delta P_s/\Delta\delta_s)}{\omega_r(Js^2 + D_p s)(\tau s + 1) + (\Delta P_s/\Delta\delta_s)} \tag{16}$$

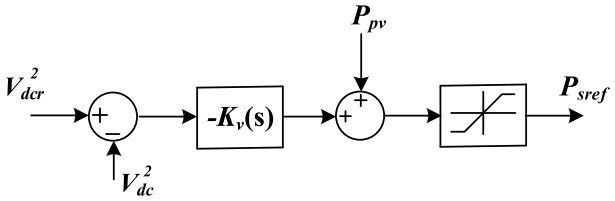

FIGURE 6. Block diagram of dc-link voltage controller.

This transfer function is also required in the dc-link voltage control design, as discussed further in the paper.

2) REACTIVE POWER LOOP

The reactive power loop regulates the excitation flux, which is done by emulating the equation given in (17).

$$\frac{d\psi_f}{dt} = \frac{1}{K}(Q_{sref} - Q_{sf} + D_q(V_{ref} - V_m)) \tag{17}$$

where, Q_{sf} is a reactive power signal Q_s which is passed through a low pass filter. The reactive power Q_s is obtained from equation (18) as given below.

$$Q_s = -1.5\omega_s \psi_{ff} i_{sq} \tag{18}$$

The reactive power loop regulates reactive power Q_s by controlling excitation flux ψ_f. The speed of response of this loop is controlled by parameter K and D_q is a drooping coefficient for voltage droop. V_m is a peak value of voltage across the shunt branch of filter and V_{ref} and Q_{sref} are reference values of V_m and Q_s.

The inner voltage generated by the synchronverter is expressed as:

$$e_s = \omega_s \psi_{ff} \tag{19}$$

This inner voltage e_s along with power angle δ_s, is treated as a reference for generating appropriate PWM pulses for VSC.

The controller diagram in Fig. 4 shows that, the reactive power loop is essential in AC voltage control. Hence, further details are discussed in the subsection ac voltage control.

B. DC-LINK VOLTAGE CONTROL

The dc-link voltage controller regulates the dc-link voltage to reference voltage V_{dcr} which is determined based on MPP or nonMPP mode of operation. It also protects the dc-link capacitor and VSC switches from overvoltage stress. Fig. 6 gives the block diagram of dc-link voltage controller. The dc-link voltage error passes through a compensator $K_v(s)$. The feedforward compensator is used to mitigate the dependencies of P_{pv} on V_{dc}, as the P_{pv} is a nonlinear function of V_{dc}. This generates a reference P_{sref}, which serves as an input to the synchronverter controller.

The dc-link voltage controller ensures that V_{dc} is maintained at V_{dcr} so that the corresponding active power gets delivered from the PV system to the grid. The following power balance equation governs this relation:

$$\frac{1}{2}C_{dc}\frac{dV_{dc}^2}{dt} = P_{pv} - P_s \tag{20}$$

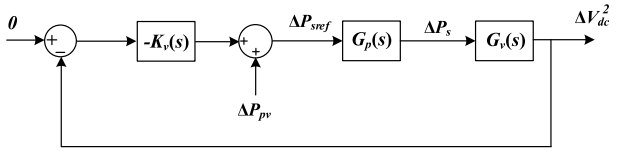

FIGURE 7. Control block diagram of designed of dc-link voltage controller.

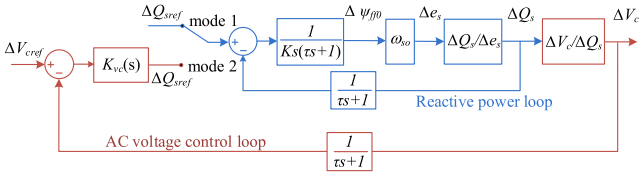

FIGURE 8. Block diagram of reactive power control loop and ac voltage control loop.

From (20), it is observed that V_{dc} is controlled by controlling P_s. Also, in single-stage PV system, PV power supply to the grid is:

$$P_{pv} = P_{cdc} + P_{loss} + P_s \tag{21}$$

where, P_{pv} is the output power of PV array, P_{cdc} is power stored in a dc-link capacitor, power loss in the inverter is denoted by P_{loss} and output power of the inverter is P_s. In equation (21), P_{cdc} and P_{loss} are very small and almost negligible. Hence, P_s can be used to control the output power of the PV array and can be used as control input in a dc-link voltage controller, as discussed in the manuscript.

The control block diagram of dc-link voltage controller is shown in Fig. 7. The transfer function $G_v(s)$ shows a relation between variation of V_{dc} with respect to output power P_s. $G_v(s)$ can be obtained from solving and linearizing equation (20) as given in [32].

$$G_v(s) = \frac{\Delta V_{dc}^2}{\Delta P_s} = -\frac{2}{C_{dc}} \frac{\frac{2L_{eq}P_{pvo}}{3V_{sd}^2}s + 1}{s} \tag{22}$$

where, L_{eq} is equivalent inductance and P_{pvo} is the initial value of P_{pv}.

To remove the impact of P_{pv} and for proper tuning of $K_v(s)$, a P_{pv} signal is used for feedforward compensation. It generates a real power reference for a synchronverter. Then it is given to active power loop $G_p(s)$ and its block diagram is shown in Fig. 5. The dc-link voltage open loop transfer function will be $l(s) = K_v(s)G_p(s)G_v(s)$, for which $K_v(s)$ is designed. Details of the controller design are discussed in the next section.

C. AC VOLTAGE CONTROL

The primary function of VSI is to supply active power to the grid, but VSI system can also be used for reactive power control and ac voltage regulation by exchanging reactive power with the grid. Fig. 8 shows the control block diagram of reactive power compensation. The reactive power controller can be operated either as a reactive power controller (i.e.,

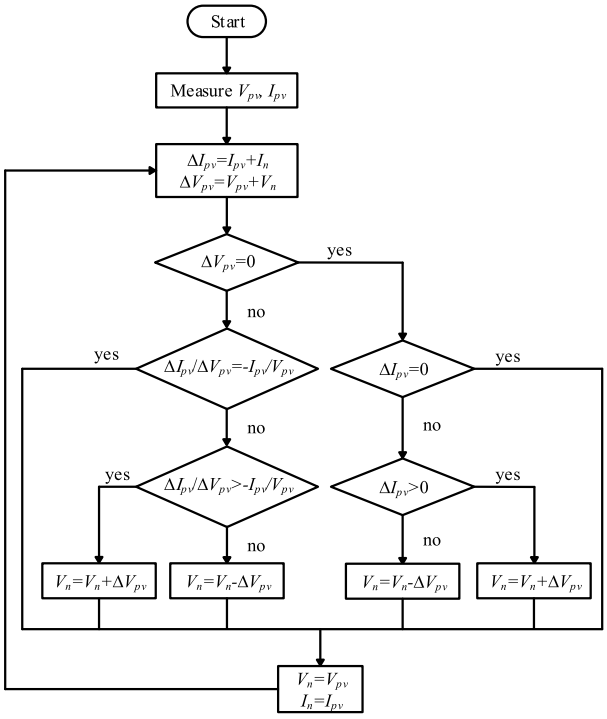

FIGURE 9. Flow chart of IC MPPT technique.

mode 1) or ac voltage controller (i.e., mode 2). The reactive power loop regulates the Q_s to Q_{sref}, which is already discussed in the above section. In ac voltage controller, the grid voltage is regulated at the desired value. The controller $K_{vc}(s)$ processes the error and generates the Q_{sref} for the reactive power loop.

In this article, voltage across filter capacitor is taken as grid voltage; hence V_c is regulated by ac voltage controller. Assume that the grid impedance is mainly inductive since $X_t \gg R_t$. Hence, resistance R_t is ignored and the voltage amplitude V_c is given as:

$$V_c = V_{pcc} + \frac{Q_s X_t}{3V_c} \tag{23}$$

where $X_t = \omega_r L_t$. Q_s is the reactive output power of VSC, and V_{pcc} is the voltage amplitude of PCC voltage. Linearizing the equation (23) and after ignoring the $2^n d$ order term to get:

$$\Delta V_c = \frac{X_t}{3(2V_c - V_{pcc})} \Delta Q_s \tag{24}$$

The PI controller $K_{vc}(s)$ is designed based on adequate phase margin and bandwidth, which is discussed in the next section. $\Delta Q_s/\Delta e_s$ is the small-signal change in reactive power to change in voltage and expression for $\Delta Q_s/\Delta e_s$ is given in the appendix.

D. MAXIMUM POWER POINT TRACKING (MPPT) SCHEME

The power generated by PV is dependent on terminal voltage V_{dc}. From the PV curve, it is observed that the power generated is nonlinear and the peak power from PV array is extracted at optimal voltage. The PV peak power and that optimal voltage point are affected by solar irradiance and temperature. Hence MPPT technique finds the optimal value of voltage at which maximum power from PV array is injected into the grid for each solar irradiance and temperature.

Many MPPT techniques are proposed in the literature [39], [40]. The most widely used methods are perturb and observation (P & O) and incremental conductance (IC). The IC is used in this article to achieve MPP and its algorithm is shown in Fig. 9. Algorithm is divided into two parts, first when change in the voltage $\Delta V_{pv} = 0$ and second when there is a change in voltage $\Delta V_{pv} \neq 0$.

When a change in ΔV_{pv} is 0, then ΔI_{pv} is checked. If ΔI_{pv} is 0, then it is assumed that the PV system is already operating at MPP and no change in voltage step is required. If the change in current is nonzero, then positive or negative voltage step change is applied depending upon the change in current is greater than zero or less than zero. As the voltage step is applied, it results in a change in current and this process continues until $\Delta I_{pv} = 0$. In second part, when ΔV_{pv} is not equal to 0, then equation $\Delta I_{pv}/\Delta V_{pv} > -I_{pv}/V_{pv}$ is examine. In IC, MPP can be tracked by regulating the difference between $\Delta I_{pv}/\Delta V_{pv}$ and I_{pv}/V_{pv}, i.e., instantaneous conductance. If the equation is satisfied, the controller assumes that there is a change in insolation or temperature and PV array is operating at MPP and no change in voltage step is required. However, if the equation is not satisfied, then the PV array is not operating at MPP and a small change in voltage is applied. This process continues until MPP operating condition is reached.

IV. CONTROLLER DESIGN

This section discusses the design of various controllers used in this system. As described above, the PV system rating is chosen as 1.4 MW. Further, the switching frequency of VSC is chosen as 6 kHz. The controllers are tuned using a SISO tool in MATLAB/SIMULINK. The design of synchronverter controller, dc-link voltage control and ac voltage control is discussed in the following subsection.

A. SYNCHRONVERTER CONTROL

1) ACTIVE POWER LOOP

In conventional power generation, loads are shared proportional to SGs ratings, and the real power injected to the grid varies according to grid frequency. This control loop is called as 'frequency droop' [8]. A prime mover maintains the rotor speed of the synchronous generator. The same mechanism is used in a synchronverter. The frequency droop mechanism is implemented by comparing ω_r and ω_s and adding a difference in T_m after multiplying by gain. From equation (13), it is observed that this gain is damping factor D_p. Hence, D_p represents as damping factor as well as frequency droop coefficient. A typical value of frequency droop is based on the change in 100% increase in real power for change in

frequency between 0.2% to 0.5%.

$$D_p = \frac{\Delta T_m}{\Delta \omega_s} \tag{25}$$

In this article, $\Delta\omega_s$ is considered to be 0.5% of ω_r.

The active power T_m is obtained from P_{sref} by dividing it by ω_r. The frequency droop in synchronverter shares the load variation with another inverter and SG in the grid. A time constant of the frequency droop loop is:

$$\tau_f = \frac{J}{D_p} \tag{26}$$

The value of τ_f is selected based on the amount of inertia provided by the synchronverter. Because large the τ_f leads to larger J and more energy storage is required to provide more inertia. Here, τ_f is chosen as 0.01s.

If a grid angle is considered a reference, then the real power provided by the synchronverter is proportional to δ_s. As a result, electromagnetic torque T_e is proportional to δ_s. Suppose the grid frequency decreases, the power angle δ_s and T_e increases. Hence the input to integral block with gain $1/J$ decreases. This results in a decrease in ω_s. This process continues till ω_s is equal to grid frequency and vice-versa when grid frequency increases.

2) REACTIVE POWER LOOP

Reactive power loop regulates the reactive power. A voltage droop controller is also a part of the reactive power loop, which ensures a sharing of the reactive power as per the rating of inverter. D_q is a voltage droop coefficient. In this article, value of the voltage droop is based on the change in 100% increase in reactive power for change in 10% of voltage. The voltage droop coefficient of voltage droop is calculated as:

$$D_q = \frac{\Delta Q_{max}}{\Delta V_s} \tag{27}$$

The voltage error is multiplied by D_q and then it is added to the error between Q_{sref} and Q_s, as shown in Fig. 4. The resulting signal is given to the integrator with a gain $1/K$ to generate ψ_f. The time constant τ_v of the voltage loop is:

$$\tau_v = \frac{K}{\omega_r D_q} \tag{28}$$

Time constant τ_v is set to be 0.02 s. Then, K is calculated as:

$$K = \tau_v \omega_r D_q \tag{29}$$

B. DC-LINK VOLTAGE CONTROL

The dc-link voltage varies because of the difference between the VSC ac terminal power P_s and P_{pv}. The power supplied by the PV source is controlled by dc-link voltage. To regulate the dc-link voltage, the compensator $K_v(s)$ processes the error $V_{dcr} - V_{dc}$ to generate P_{sref} for synchronverter. The structure of the $K_v(s)$ is given below in equation (30) [32]. This compensator generates enough phase margin for a given bandwidth [22]

$$K_v(s) = \frac{1}{s}\beta_1 \frac{(s + \frac{\beta_2}{\beta_3})^2}{(s + \beta_2)^2} \tag{30}$$

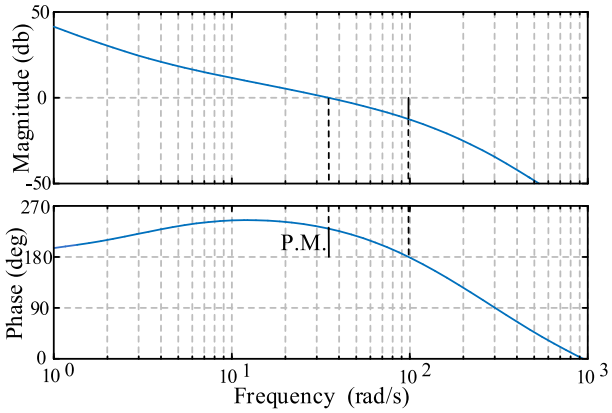

FIGURE 10. Bode plot of compensated and uncompensated dc-link voltage control loop.

where, β_1, β_2 and β_3 are the parameters of controller $K_v(s)$.

The control block diagram of dc-link voltage controller is shown in Fig. 7. The dc-link voltage open loop transfer function will be $l(s) = K_v(s)G_p(s)G_v(s)$, for which $K_v(s)$ is designed for desired gain margin and phase margin. The open loop transfer function of dc-link controller is as follows:

$$H_{dc}(s) = K_v(s)\frac{\Delta V_{dc}^2}{\Delta P_s} = -\frac{2}{C_{dc}}\frac{\frac{2L_{eq}P_{pvo}}{3V_{sd}^2}s + 1}{s}\frac{\Delta P_s}{\Delta P_{sref}} \tag{31}$$

The $K_v(s)$ is multiplied by -1 to compensate the negative sign of $G_v(s)$. The controller is designed for the worst case by considering negative P_{pvo}. To regulate V_{dc}, $K_v(s)$ is designed with 50^o phase margin at 35 rad/s bandwidth. $K_v(s)$ consists of an integrator to achieve zero steady state error. Further, the gain is added in $K_v(s)$ to achieve gain cross over frequency at 35 rad/sec. A lead compensator is added in $K_v(s)$ to stabilize the uncompensated loop with 50^o phase margin at 35 rad/s bandwidth. The bode plot with the compensated loop is shown in Fig. 10.

C. AC VOLTAGE CONTROL

The control block diagram of ac voltage control is shown in Fig. 8. The open loop transfer function of the ac voltage controller is as follows:

$$H_{vc}(s) = \frac{K_{vc}(s)\omega_{so}(\Delta Q_s/\Delta e_s)}{Ks(\tau s + 1)(\tau s + 1) + \omega_{so}(\Delta Q_s/\Delta e_s)}\frac{\Delta V_c}{\Delta Q_s} \tag{32}$$

where,

$$K_{vc}(s) = \frac{k_{pvc}s + k_{ivc}}{s} \tag{33}$$

The PI controller $K_{vc}(s)$ is used to regulate the voltage V_c. k_{pvc} and k_{ivc} are proportional gain and integral gain of the PI controller, respectively

The compensated bode plot of the ac voltage controller is shown in Fig. 11. It is noted that the ac voltage control loop includes an inner loop, which is a reactive power loop. Therefore, the dynamics of the outer loop are slower than the inner loop. Hence, the controller is designed for a phase margin of 85^o and cross over frequency of 10 rad/s.

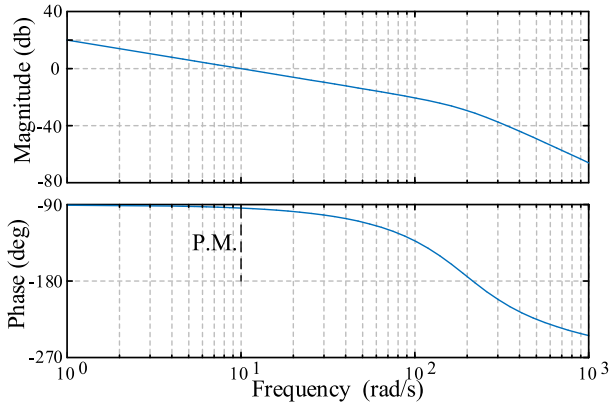

FIGURE 11. Bode plot of compensated ac voltage controller.

TABLE 1. System parameters.

Parameter	Value	Parameter	Value
PV rated capacity	1.4 MW	J	28.37 kg.m^2
Source voltage(L-L)	0.4 kVrms	D_p	2837 N.m.s/rad
PCC voltage(L-L)	12.47 kVrms	K	270.444 kVar.rad/V
V_{dc}	800 V	D_q	43.042 kVar/V
C_{dc}	1000 mf	K_{pvc}	1
R_f	0.002 Ω	K_{ivc}	1.6091x10^6
L_f	100 mH	β_1	1.5211x10^5
R_d	0.1 Ω	β_2	258.52
C_f	7000 μf	β_3	58.13
L_t	0.1 pu	τ	0.002 s
Transformer rating	1.5 MVA	Rated frequency	50 Hz

V. SIMULATION RESULTS

This section presents the response of a synchronverter based 1.4 MW PV system connected to the North American MV network. The MPP voltage of the PV array is 800V. The PV junction temperature of PV system is considered to be 25^oC.

The PV system parameters and controllers are given in Table 1. The North American MV benchmark network parameters are given in [25].

A. CASE I: PV SYSTEM RESPONSE WITHOUT MPPT

This case study shows the PV system response to the stepwise change in solar irradiation G and dc-link voltage setpoint V_{dcr} when the MPPT scheme is disabled. Fig. 12 shows the PV system response.

Initially, when the PV system starts, V_{dc} is regulated to 900V, and G is taken as 0.6 kW/m^2. At $t = 6$ s, V_{dcr} changes from 900V to 950V, resulting in a PV system output power reduction, as shown in Fig. 12. At $t = 9$ s, G changes to 1 kW/m^2 from 0.6 kW/m^2, which increases the PV system output power. The case study shows the need of MPPT technique and it is noted that PV power generation is approximately proportional to available solar irradiation.

B. CASE II: PV SYSTEM RESPONSE WITH MPPT

The IC MPPT technique is used to track maximum power for the available irradiance. The response of the system is

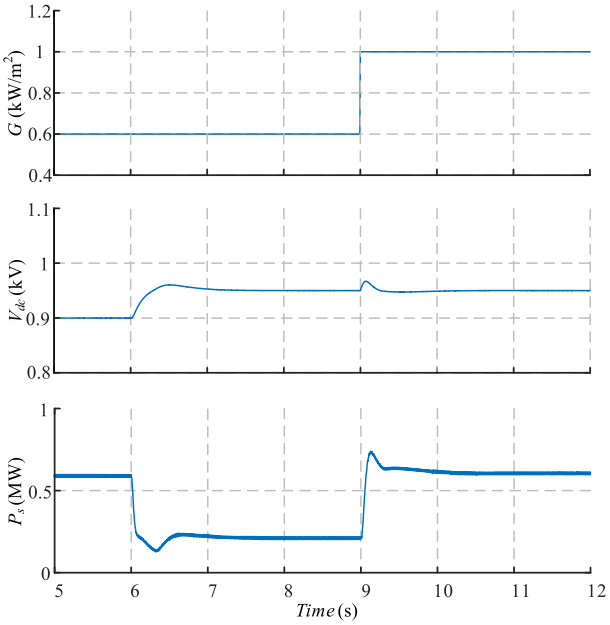

FIGURE 12. PV system response to stepwise changes in solar irradiation and dc-link voltage setpoint without MPPT.

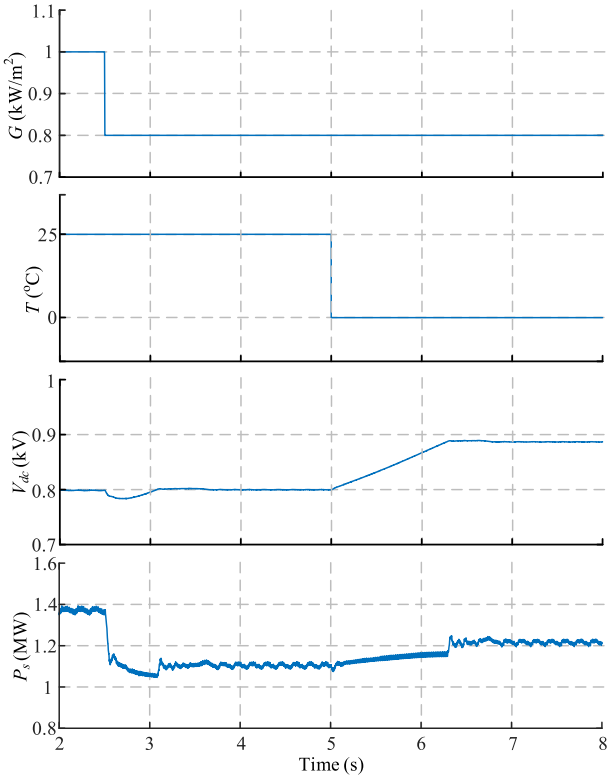

FIGURE 13. PV system response to stepwise changes in solar irradiation and temperature, with the MPPT.

observed for a step change in solar irradiance G and PV junction temperature T.

Initially, G is at 1 kW/m^2, and V_{dc} is at its MPP, i.e., 800V and PV System output is 1.4 MW. At $t = 2.5$s, G changes

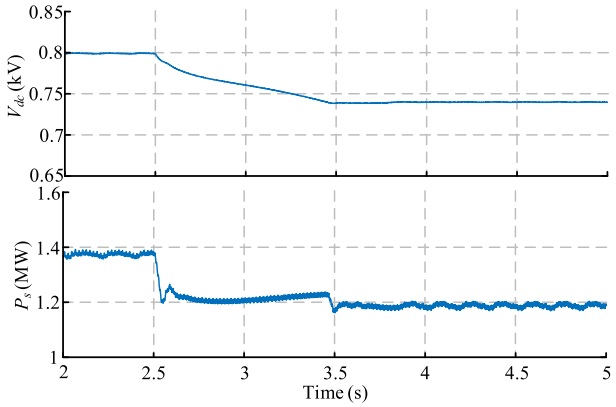

FIGURE 14. PV system response to partial shading condition.

to 0.8 kW/m^2, then the output power changes to 1.1 MW. The junction temperature T is then changed to 0^oC at 5 s and due to this, constant rise is observed in the dc-link voltage V_{dc} and output power P_s of the inverter. After a change in T, V_{dc} becomes 0.88 kV to track the maximum power of 1.22 MW related to that temperature. It is observed that the temperature change has a significant impact on PV system operating points, as shown in Fig. 13.

The performance of PV system for partial shading conditions is shown in Fig. 14. Initially, PV operates in MPPT mode with available rated irradiations $G = 1$ kW/m^2 and the entire array receives uniform irradiations. Before $t = 2.5$s, V_{dc} is at rated MPP and VSI provide rated power P_s to distribution system. At $t = 2.5$s, sudden change in ambient conditions occurs, which causes partial shading of the array and the insolation level of shaded module decreases. Nonuniform shading of the PV array reduces output current and voltage of the PV system. MPPT technique detects the partial shading, which leads to decrease in voltage V_{dc} and output power P_s of VSI as shown in Fig. 14. V_{dc} settles at new MPP, i.e., 0.74 kV and P_s decreases to 1.2 MW. As per PV curve shown in Fig. 3, the power generated by PV panel at 0.74 kV is 1.36 MW; but because of the partial shading effect, V_{mpp} and I_{mpp} reduce, and P_s decreases to 1.2 MW. Also, it observes that the system is stable after the partial shading disturbance.

C. CASE III: INFLUENCE OF PV-SYNCHRONVERTER ON BENCHMARK SYSTEM

This test is carried out with and without PV system to check the effect of connecting a synchronverter to the benchmark system. In the benchmark system, highest load is connected to bus 1. The test is carried out by disconnecting a load on bus 1. Its effect on PCC frequency is observed on bus 3, where the PV system is connected. Initially, G is set to 1 kW/m^2 and $Q_{sref} = 0$ VAR. Load at bus 1 is disconnected at $t = 4$s.

Fig. 15 shows the test results without PV system and with PV system. A load is disconnected at $t = 4$s. A current drawn from the grid source decreases when a load is disconnected,

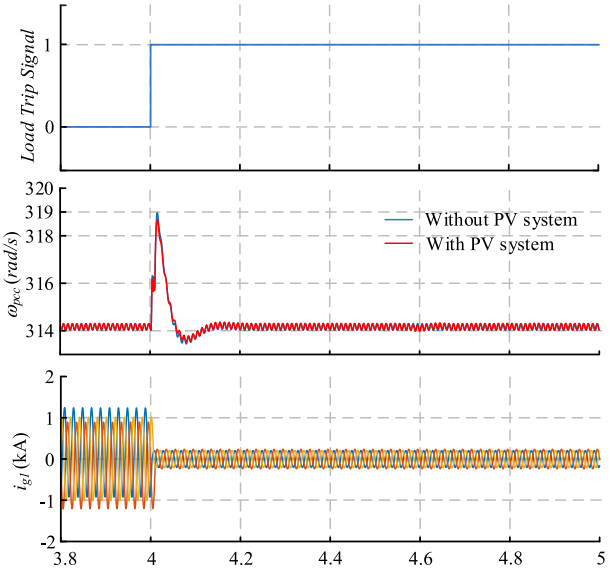

FIGURE 15. System response for chnage in load without PV system and with PV system.

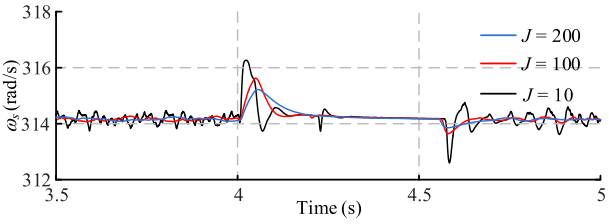

FIGURE 16. Frequency response for change in load at different value of J.

as shown in Fig. 15. The effect of connecting synchronverter based PV system is clearly observed from the frequency waveform at PCC. Though overall power increases in the benchmark system, due to inertia provided by the PV system, the overshoot of frequency with PV systm at bus 3 is shown in Fig. 15. is slightly less compared to overshoot in frequency without a PV system.

D. CASE IV: FREQUENCY RESPONSE OF PV SYSTEM AT DIFFERENT J

This study investigates the response of PV system frequency ω_s for different values of J when a load is disconnected from bus1. The load is disconnected at $t = 4$s. It is observed from Fig. 16 that as the inertia increases, the overshoot of frequency ω_s decreases. Also, the increase in control parameter J reduces the RoCoF, as observed from Fig. 16.

E. CASE V: PV SYSTEM RESPONSE FOR MPP AND nonMPP MODE

The operation of PV system for change in G with nonMPP mode is given in [22] and it is observed that the PV system provides virtual inertia in nonMPP mode. Following this, this case study will conduct a test with the distribution system. Power generated by the PV system is same for MPP and

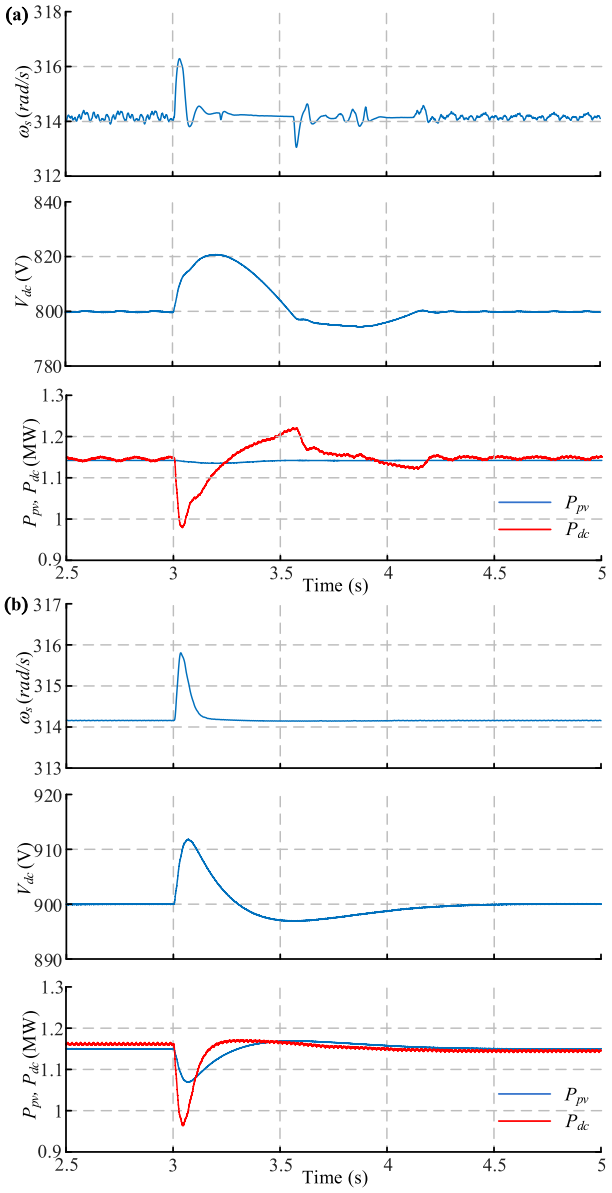

FIGURE 17. System response for change in load with (a) MPP mode (b) nonMPP mode.

nonMPP modes of operation. Initially, for MPP mode $G = 0.8$ kW/m^2 and for nonMPP mode, available irradiation is 1 kW/m^2 with regulated dc-link voltage to 900V. A disturbance is created by disconnecting the load at $t = 3$s.

From Fig. 17 (a), it is observed that there is no change in P_{pv}, when a disturbance occurs as the PV system is operating at MPP mode. For the nonMPP case, the drop in P_{pv} is observed in response to disturbance, as shown in Fig. 17 (b). This results in less overshoot of frequency ω_s in case of nonMPP mode compared to MPP mode. Inertia provided by the PV system is based on the PV curve as shown in Fig. 3. As per the PV curve, at MPP, a small change in V_{dc} cannot make more change in the output power of PV. However, when the PV system operates in nonMPP mode (negative slope of PV curve), the small change in V_{dc} affects the PV output power. In this way, the PV system participates in virtual inertia during nonMPP mode.

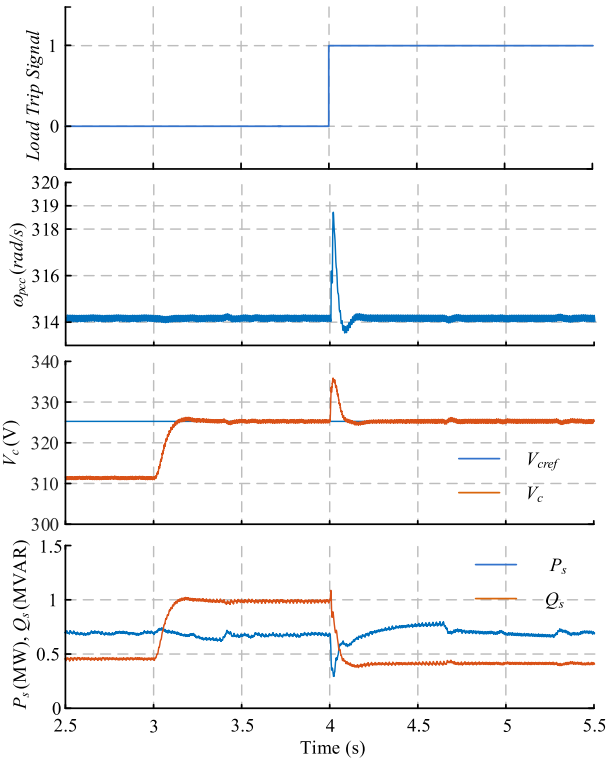

FIGURE 18. System response for change in load with ac voltage regulator.

F. CASE VI: PV SYSTEM RESPONSE WITH AC VOLTAGE REGULATOR

This test observes the response of a synchronverter when exchanging active as well as reactive power for change in total load. Initially, G is set to 1 kW/m^2 and reactive power controller is activated with Q_{sref} set to 0 kVAR. The ac voltage controller is activated at $t = 3$s and the load at bus1 is disconnected at $t = 4$s.

Initially, Q_{sref} is set to 0 kVAR, though some reactive power is injected into the grid; because of the filter capacitor and activated voltage droop as shown in Fig. 18. As the V_c is not equal to V_{sref}, some value is added due to voltage droop in reactive power error and that is why reactive power is injected in the grid. At $t = 3$s, ac voltage controller is activated, as the V_{cref} is set to 325.26 V, V_c start tracking V_{cref} and settle at 325.26 V. To increase the voltage, more reactive power is injected into the grid, which is observed from Q_s. The change in V_c does not affect the active power output P_s and P_s is same in steady state. The V_c keeps tracking V_{cref} after a load is disconnected. As the total load decreases, less reactive power Q_s is injected into the grid to regulate voltage. Also, overshoot in frequency ω_{pcc} is less than the test result shown in Fig. 15 due to inertia provided by the dc-link capacitor.

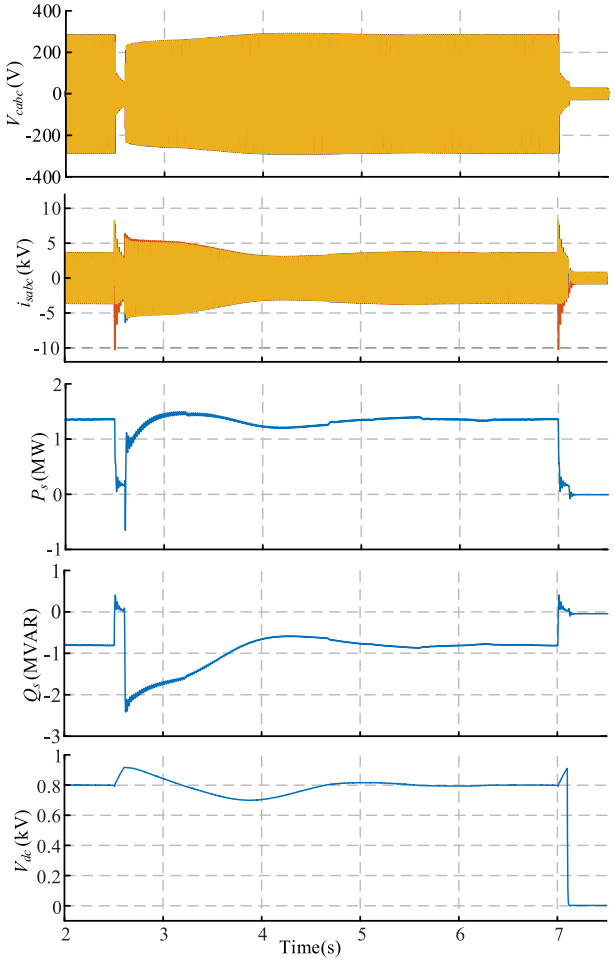

FIGURE 19. PV system response to a three-phase-to-ground network fault at bus4, without voltage droop mechanism.

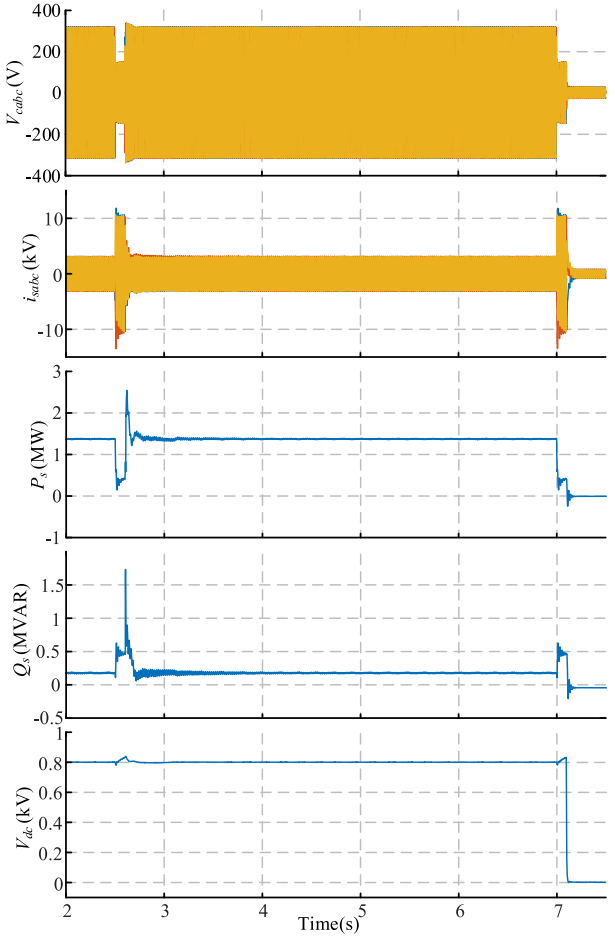

FIGURE 20. PV system response to a three-phase-to-ground network fault at bus 4, with voltage droop mechanism.

G. CASE VII: PV SYSTEM RESPONSE WITH AC VOLTAGE REGULATOR (THREE PHASE TO GROUND FAULT)

This case studies the response of PV system for symmetric fault. The fault is created at bus 4, as shown in Fig. 1. Initially, G is at 1 kW/m^2. A MPPT scheme determines the dc-link voltage. The response of a synchronverter without considering voltage droop mechanism is shown in Fig. 19. A temporary fault is created at $t = 2.5$ s, for the duration 0.1 s. As the fault is symmetric, the magnitude of output current of VSI 'i_{sabc}' increases equally and a voltage across capacitor V_{cabc} drops equally. As the PCC voltage drops after fault, output power P_s of VSI decreases and the dc-link voltages V_{dc} increase due to power imbalance between PV and grid. Due to change in voltage V_{cabc}, reactive power Q_s is disturbed and its response is same as V_{cabc}. After clearing the fault, dc-link voltage is back to its MPP value; hence, P_s also regains its original value. As the fault is symmetric, V_{cabc} and i_{sabc} are symmetric during a fault, as shown in Fig. 19. As the fault is only for 0.1 sec, the PV system is still connected to the grid. If a fault is longer than 0.16s, the PV system gets disconnected from the grid as per IEEE 1547-2003 guidelines. A permanent fault is created at 7s and after 0.16s PV system is disconnected from the grid, as shown in Fig. 19.

Fig. 20 shows the response of the system for symmetric fault considering the voltage droop mechanism in the reactive power loop. The initial conditions and operation sequence are same as in the above case. As the magnitude of V_{cabc} drops after fault, due to the presence of voltage droop, to regulate voltage V_{cabc} the output reactive power increases, resulting in increased i_{sabc} till the fault is not cleared and it is shown in Fig. 20. It is also observed that, a settling time of Q_s decreases due to voltage droop. Also, a synchronverter tries to maintain the voltage and due to that, less impact on V_{dc} is observed.

H. CASE VIII: PV SYSTEM RESPONSE WITH ASYMMETRIC FAULT

This case demonstrates the response of two asymmetric faults 1) single phase to ground fault 2) line to line fault. For both the cases, initially, PV is operating in MPPT mode, and the power provided by PV corresponds to $G = 0.8$ kW/m^2. Also, the voltage droop mechanism is active in the reactive power loop with Q_{sref} set to 0.

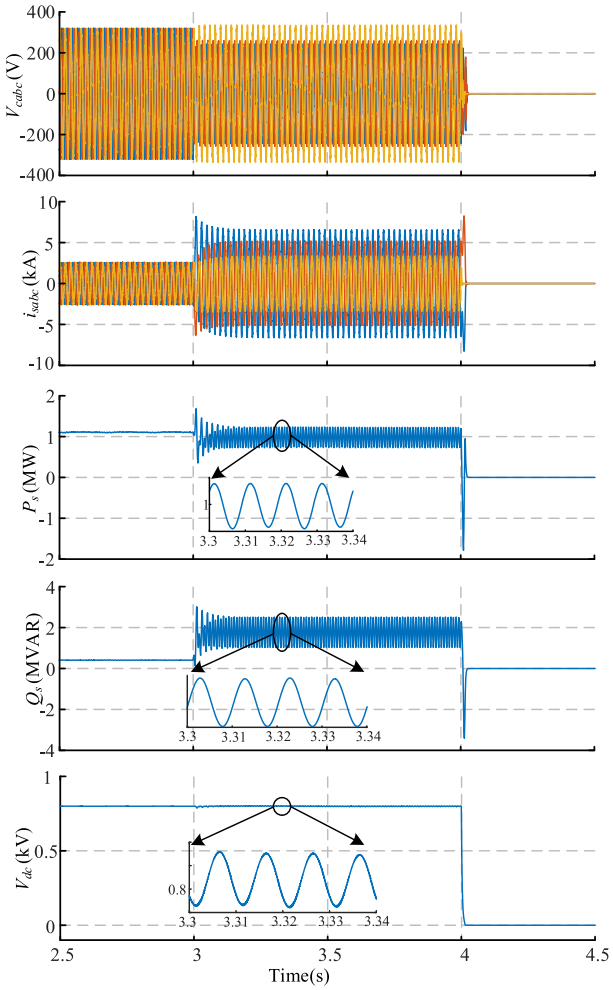

FIGURE 21. PV system response to a single-phase-to-ground fault at bus 4.

Fig. 21 shows the repones of PV system for single phase to ground fault. The permeant fault occurs at phase A on bus 4 at $t = 3$ s. Due to the voltage source nature of the PV system, the unbalance form of inverter output current i_{sabc} is observed, as shown in Fig. 21. Also, a drop in the inverter output voltage V_{cabc} is observed, and this drop is in a and b phase due to delta connection on the low voltage side of a transformer. Such faults result in double frequency pulsation in PV system output power P_s. These pulsations are also observed in dc-link voltage V_{dc}, P_s and Q_s. After 0.16s as the fault is not cleared, hence the PV system is disconnected from the grid.

Fig. 22 shows the repones of PV system for line-to-line fault. The other condition for this case is same as in single phase to ground fault. Fig. 22 shows same nature of response as shown in the previous case. It is observed that during a fault, increase in current is more than single phase to a ground fault; hence, this fault is more severe than single phase to ground fault. These faults also result in double frequency pulsation in the PV system.

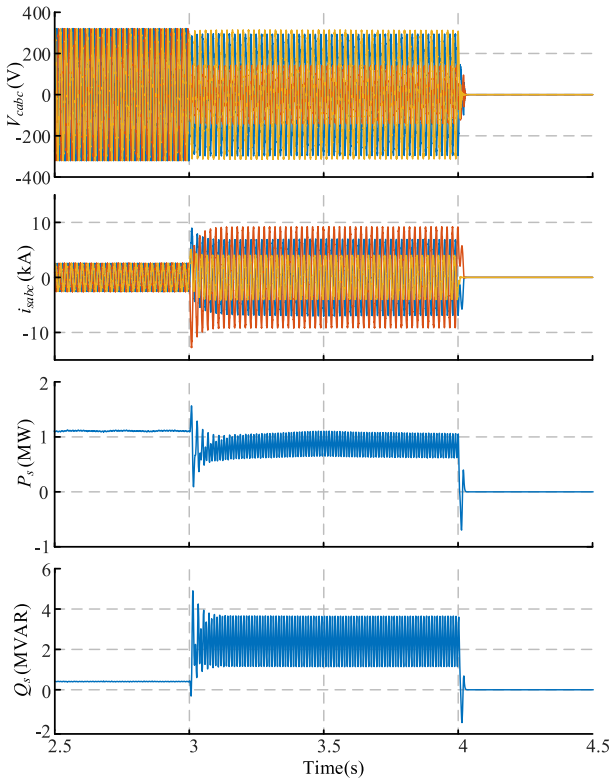

FIGURE 22. PV system response to a line-to-line fault at bus 4.

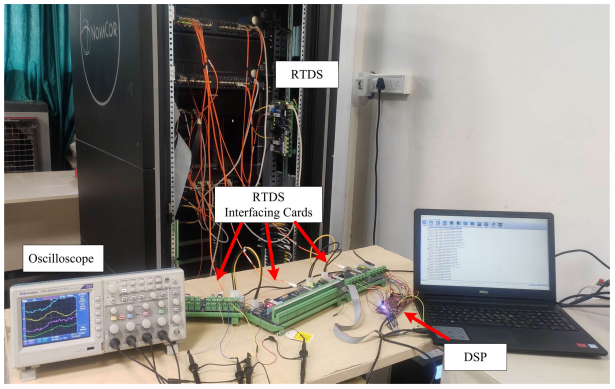

FIGURE 23. CHIL implementation setup.

VI. CHIL RESULTS

This section validates the simulation results with CHIL results. The CHIL implementation test setup contains RTDS [41] and controller TMS320F28377s, as shown in Fig 23. The Real-Time Digital Simulator (RTDS) is a digital power system processing hardware architecture to model the study power system in real-time. The RTDS is utilized with real-time simulation software, RSCAD. The power part is modeled in RSCAD software. The models of inverter and other power components in RTDS are based on the Dommels algorithm [41]. A large portion of power components are simulated in a large time step of 25-50μs called mainstep. The power electronics component operate at higher frequencies

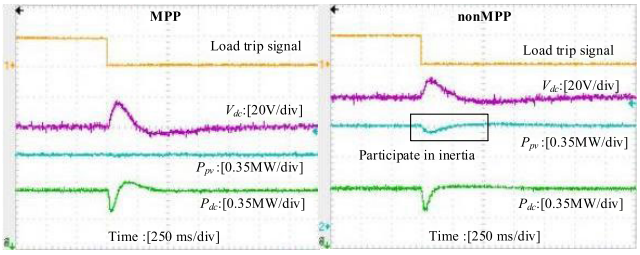

FIGURE 24. System response for chnage in load at MPP and nonMPP PV operating modes.

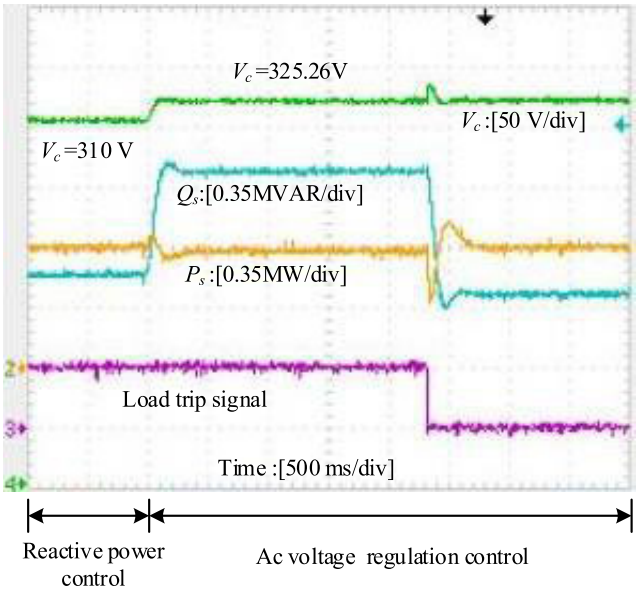

FIGURE 25. System response for chnage in load with ac voltage regulation.

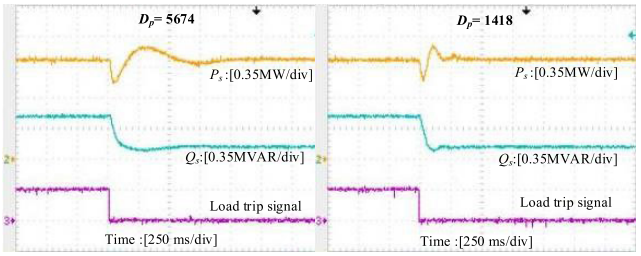

FIGURE 26. PV system response for chnage in load at value of different D_p.

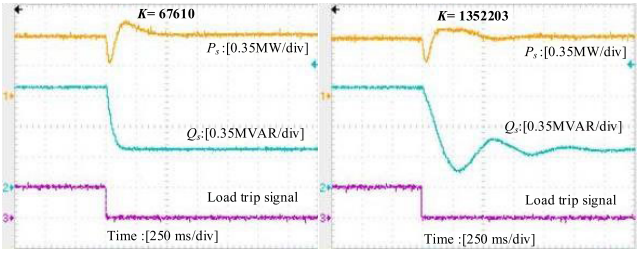

FIGURE 27. PV system response for chnage in load at different K with reactive power control.

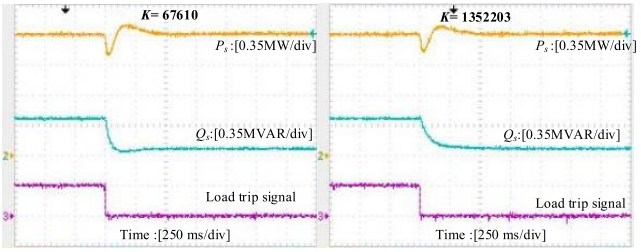

FIGURE 28. PV system response for chnage in load at different K with ac voltage regulation.

are run in a substep environment, having time step 1-4μs. The CHIL tests are conducted considering the minimum time step. The control part is programmed in digital signal processing (DSP) based unit TMS320D28377s. The sampling time of Analog-to-digital converter of microprocessor is considered 0.1ms. System parameters used to carry out tests are same as simulation results and are given in Table 1.

The CHIL tests are carried out for MPP and nonMPP modes, as shown in Fig. 24. The initial conditions and disturbance created by a change in load are same as given in simulation of case V (Fig. 17). From the P_{pv}, it is observed that during nonMPP mode with ES, PV also participates in providing inertia, which is not observed in the MPP mode of operation.

The PV system response for ac voltage regulation control is validated with CHIL results, as shown in Fig. 25. The initial conditions and triping sequence of the test are same as that of simulation of case VI (Fig. 18). Initially, the PV system is operating in reactive power mode. When ac voltage regulation mode is activated, V_c starts tracking V_{cref}, which is 325.26 V by operating the PV system in capacitive mode. The active power injected by the PV system is less as the available solar irradiation is less; hence the remaining capacity of PV system can be used for injecting/absorbing reactive power to increase the efficiency of PV system. As the load connected at bus 1 is disconnected, the voltage drop is reduced and hence the reactive power injected to regulate the voltage is reduced.

Response of the PV system for change in D_p is shown in Fig. 26. Initially $G = 8$ kW/m^2, Q_{sref} is set to 0 MVAR and disturbance is created by disconnecting the load on bus 1. As mentioned in the literature, as D_p increases, the damping of the system increases. For $D_p = 5674$, systems damping is more than $D_p = 1418$, as observed from Fig. 26. The impact is also observed on Q_s due to the coupling of active and reactive power loops.

The reactive power loop parameter K affects the system response, and it is observed from Fig. 27. Initially, $G = 1$ kW/m^2, and the reactive power loop is activated with $Q_{sref} = 0$ MVAR. The disturbance is created by disconnecting load on bus 1. Increase in response of the system is observed for higher value of K and its little impact is also observed on P_s.

$$\frac{\Delta P_s}{\Delta \delta_s} = \frac{3(-e_s^2 R_f sin(2\delta_s) + e_s V_{cd} R_f sin(\delta_s) + e_s^2 X_f cos(2\delta_s) + e_s V_{cq} X_f sin(\delta_s))}{2(R_f^2 + X_f^2)} + \frac{3(e_s^2 R_f^3 sin(2\delta_s) - 2e_s V_{cd} R_f^3 sin(\delta_s) - e_s^2 R_f^2 X_f cos(2\delta_s) - e_s V_{cq} R_f^2 X_f sin(\delta_s) + e_s V_{cd} R_f^2 X_f cos(\delta_s) + e_s^2 R_f X_f^2 sin(2\delta_s) - 2e_s V_{cd} R_f X_f^2 sin(\delta_s) - e_s^2 X_f^3 cos(2\delta_s) - e_s V_{cq} X_f^3 sin(\delta_s) + e_s V_{cd} X_f^3 cos(\delta_s))}{2(R_f^2 + X_f^2)^2} \quad (34)$$

$$\frac{\Delta Q_s}{\Delta e_s} = \frac{3(2e_s X_f cos(\delta_s^2) - V_{cd} X_f cos(\delta_s) - 2e_s R_f sin(\delta_s) cos(\delta_s) + V_{cq} R_f cos(\delta_s))}{2(R_f^2 + X_f^2)} + \frac{3(-2e_s R_f^2 X_f cos(\delta_s^2) + 2V_{cd} R_f^2 X_f cos(\delta_s) + 2e_s X_f^2 R_f sin(\delta_s) cos(\delta_s) - V_{cq} X_f^2 R_f cos(\delta_s) - V_{cd} X_f^2 R_f sin(\delta_s) + 2e_s R_f^3 sin(\delta_s) cos(\delta_s) - V_{cd} R_f^3 sin(\delta_s) - V_{cq} R_f^3 cos(\delta_s) - 2e_s X_f^3 cos(\delta_s^2) + 2V_{cd} X_f^3 cos(\delta_s))}{2(R_f^2 + X_f^2)^2} \quad (35)$$

Response of the system for change in K is observed when the ac voltage regulation loop is activated, as shown in Fig. 28. Initially, G is set to 0.5 kW/m^2 and disturbance is created same as above test. As the K increases, the time constant τ_v increases and for $K = 1352203$, the τ_v is near to bandwidth of ac voltage regulation controller. Hence, the response for a lower value of K is smooth compared to a higher value of K.

VII. POSSIBLE FUTURE EXTENSIONS OF THE PRESENT WORK

It is clearly evident from the literature that the grid forming control approach will be a promising solution as the share of renewable energy increases in the existing power system. Therefore, a preliminary simulation study on synchronverter controlled PV inverter connected to MV benchmark system is carried out in this paper. As discussed earlier, Synchronverter is one of the various grid forming techniques. However, there are several techniques like droop control, VSM, EDPC, VOC, SPC. Along with the development of grid forming techniques, it is important to study these techniques on different benchmark systems. A study should be carried out from the point of view of frequency regulation, amount of PV power penetration, how effectively it contributes to system strength, etc. Also, a study of control techniques from steady-state and dynamic stability perspectives will be a significant study along with the comparison of control techniques from different aspects.

VIII. CONCLUSION

This article presented the performance of a PV synchronverter with a North American MV benchmark system. The controllers like synchronverter, dc-link voltage control and ac voltage control are described in detail. The design and tuning of these controllers are presented. The results revealed that for the load change disturbance, PCC frequency overshoot is observed to be marginally lesser with the PV system as compared to the system without PV. The PV system response for grid side disturbances during MPP and nonMPP mode was studied. It is observed that the inverter frequency overshoot is slightly less in nonMPP mode compared to MPP mode. The voltage profile of distribution system is improved when the PV system is operated in ac voltage regulation mode and regulates voltage with a fast dynamic response. Furthermore, the response of synchronverter for fault analysis was studied in detail along with the voltage droop mechanism. It is observed that the overall response reaches quite faster to steady state with active voltage droop mechanism. Simulation of the nonlinear model is performed in PSCAD/EMTDC. The CHIL carried out with RTDS validates the simulation results, which are consistent with the simulation results.

APPENDIX

The detailed derivation of $\Delta P_s/\Delta \delta_s$ and $\Delta Q_s/\Delta e_s$ is given in [22]. Equation of $\Delta P_s/\Delta \delta_s$ and $\Delta Q_s/\Delta e_s$ are given in (34) and (35), as shown at the top of the page.

REFERENCES

[1] H. L. Willis and W. G. Scott, *Distributed Power Generation: Planning and Evaluation*. New York, NY, USA: Marcel-Dekker, 2000.

[2] C. Schauder, "Advanced inverter technology for high penetration levels of PV generation in distribution systems," NREL Subcontract Rep., Golden, CO, USA, Tech. Rep. NREL/SR- 5D00-60737, 2014.

[3] A. D. Falehi, "An innovative OANF–IPFC based on MOGWO to enhance participation of DFIG-based wind turbine in interconnected reconstructed power system," *Soft Comput.*, vol. 23, no. 23, pp. 12911–12927, Dec. 2019.

[4] A. D. Falehi, "Half-cascaded multilevel inverter coupled to photovoltaic power source for AC-voltage synthesizer of dynamic voltage restorer to enhance voltage quality," *Int. J. Numer. Modelling: Electron. Netw., Devices Fields*, vol. 34, no. 5, p. e2883, Aug. 2021.

[5] J. Rocabert, A. Luna, F. Blaabjerg, and P. Rodríguez, "Control of power converters in AC microgrids," *IEEE Trans. Power Electron.*, vol. 27, no. 11, pp. 4734–4749, Nov. 2012, doi: 10.1109/TPEL.2012.2199334.

[6] A. Yazdani, A. R. Di Fazio, H. Ghoddami, M. Russo, M. Kazerani, J. Jatskevich, K. Strunz, S. Leva, and J. A. Martinez, "Modeling guidelines and a benchmark for power system simulation studies of three-phase single-stage photovoltaic systems," *IEEE Trans. Power Del.*, vol. 26, no. 2, pp. 1247–1264, Apr. 2011, doi: 10.1109/TPWRD.2010.2084599.

[7] Y. Lin, J. H. Eto, B. B. Johnson, J. D. Flicker, R. H. Lasseter, H. N. V. Pico, G.-S. Seo, B. J. Pierre, and A. Ellis, "Research roadmap on grid-forming inverters," Nat. Renew. Energy Lab., Golden, CO, USA, Tech. Rep. NREL/TP-5D00-73476, 2020.

[8] D. B. Rathnayake, M. Akrami, C. Phurailatpam, S. P. Me, S. Hadavi, G. Jayasinghe, S. Zabihi, and B. Bahrani, "Grid forming inverter modeling, control, and applications," *IEEE Access*, vol. 9, pp. 114781–114807, 2021, doi: 10.1109/ACCESS.2021.3104617.

[9] P. Unruh, M. Nuschke, P. Strauß, and F. Welck, "Overview on grid-forming inverter control methods," *Energies*, vol. 13, no. 10, p. 2589, May 2020.
[10] A. D. Falehi, "An innovative optimal RPO-FOSMC based on multi objective grasshopper optimization algorithm for DFIG-based wind turbine to augment MPPT and FRT capabilities," *Chaos, Solitons Fractals*, vol. 130, Jan. 2020, Art. no. 109407.
[11] Y. Sahri, S. Tamalouzt, and L. S. Belaid, "Enhanced direct power control strategy of a DFIG-based wind energy conversion system operating under random conditions," in *Period. Polytech. Electr. Eng. Comput.*, vol. 65, no. 3, pp. 196–206, 2021, doi: 10.3311/PPee.16656.
[12] U. Tamrakar, D. Shrestha, M. Maharjan, B. Bhattarai, T. Hansen, and R. Tonkoski, "Virtual inertia: Current trends and future directions," *Appl. Sci.*, vol. 7, no. 7, p. 654, Jun. 2017.
[13] K. M. Cheema, "A comprehensive review of virtual synchronous generator," *Int. J. Electr. Power Energy Syst.*, vol. 120, Sep. 2020, Art. no. 106006.
[14] H.-P. Beck and R. Hesse, "Virtual synchronous machine," in *Proc. 9th Int. Conf. Electr. Power Quality Utilisation*, Oct. 2007, pp. 1–6.
[15] K. R. Vasudevan, V. K. Ramachandaramurthy, T. S. Babu, and A. Pouryekta, "Synchronverter: A comprehensive review of modifications, stability assessment, applications and future perspectives," *IEEE Access*, vol. 8, pp. 131565–131589, 2020, doi: 10.1109/ACCESS.2020.3010001.
[16] B. Barac, M. Krpan, T. Capuder, and I. Kuzle, "Modeling and initialization of a virtual synchronous machine for power system fundamental frequency simulations," *IEEE Access*, vol. 9, pp. 160116–160134, 2021, doi: 10.1109/ACCESS.2021.3130375.
[17] Q.-C. Zhong and G. Weiss, "Synchronverters: Inverters that mimic synchronous generators," *IEEE Trans. Ind. Electron.*, vol. 58, no. 4, pp. 1259–1267, Apr. 2011.
[18] Q.-C. Zhong, P.-L. Nguyen, Z. Ma, and W. Sheng, "Self-synchronized synchronverters: Inverters without a dedicated synchronization unit," *IEEE Trans. Power Electron.*, vol. 29, no. 2, pp. 617–630, Feb. 2014, doi: 10.1109/TPEL.2013.2258684.
[19] J. Fang, H. Li, Y. Tang, and F. Blaabjerg, "On the inertia of future more-electronics power systems," *IEEE J. Emerg. Sel. Topics Power Electron.*, vol. 7, no. 4, pp. 2130–2146, Dec. 2019.
[20] H. Wu, X. Ruan, D. Yang, X. Chen, W. Zhao, Z. Lv, and Q.-C. Zhong, "Small-signal modeling and parameters design for virtual synchronous generators," *IEEE Trans. Ind. Electron.*, vol. 63, no. 7, pp. 4292–4303, Jul. 2016.
[21] S. Dong and Y. C. Chen, "Adjusting synchronverter dynamic response speed via damping correction loop," *IEEE Tran Energy Convers.*, vol. 32, no. 2, pp. 608–619, Jun. 2017.
[22] A. J. Sonawane and A. C. Umarikar, "Small-signal stability analysis of PV-based synchronverter including PV operating modes and DC-link voltage controller," *IEEE Trans. Ind. Electron.*, early access, Sep. 8, 2021, doi: 10.1109/TIE.2021.3109506.
[23] K. Y. Yap, C. R. Sarimuthu, and J. M.-Y. Lim, "Grid integration of solar photovoltaic system using machine learning-based virtual inertia synthetization in synchronverter," *IEEE Access*, vol. 8, pp. 49961–49976, 2020, doi: 10.1109/ACCESS.2020.2980187.
[24] L. He, Z. Shuai, X. Zhang, X. Liu, Z. Li, and Z. J. Shen, "Transient characteristics of synchronverters subjected to asymmetric faults," *IEEE Trans. Power Del.*, vol. 34, no. 3, pp. 1171–1183, Jun. 2019, doi: 10.1109/TPWRD.2019.2906766.
[25] *CIGRE Technical Brochure, Task Force C6.04.02, Benchmark Systems for Network Integration of Renewable and Distributed Energy Resources*, CIGRE, Paris, France, 2011.
[26] P. Kotsampopoulos, D. Lagos, N. Hatziargyriou, M. O. Faruque, G. Lauss, O. Nzimako, P. Forsyth, M. Steurer, F. Ponci, A. Monti, and V. Dinavahi, "A benchmark system for hardware-in-the-loop testing of distributed energy resources," *IEEE Power Energy Technol. Syst. J.*, vol. 5, no. 3, pp. 94–103, Sep. 2018, doi: 10.1109/JPETS.2018.2861559.
[27] R. C. Neville, *Solar Energy Conversion: The Solar Cell*, 2nd ed. New York, NY, USA: Elsevier, 1995.
[28] J. A. Gow and C. D. Manning, "Devolpment of a photovoltaic array model for use in power-electronics simulation studies," in *Proc. Inst. Electt. Eng., Elect. Power Appl.*, vol. 146, no. 2, pp. 193–200, 1999.
[29] K. Nishioka, N. Sakitani, Y. Uraoka, and T. Fuyuki, "Analysis of multicrystalline silicon solar cells by modified 3-diode equivalent circuit model taking leakage current through periphery into consideration," *Sol. Energy Mater. Sol. Cells*, vol. 91, no. 13, pp. 1222–1227, Aug. 2007.
[30] S. A. Rahman, R. K. Varma, and T. Vanderheide, "Generalised model of a photovoltaic panel," *IET Renew. Power Generat.*, vol. 8, no. 3, pp. 217–229, Apr. 2014.
[31] S. B. Subramanian, "State space modeling of smart PV inverter as STATCOM (PV-STATCOM) for voltage control in a distribution system," M.S. thesis, Elect. Comput. Eng., Univ. Western Ontario, London, ON, Canada, 2016.
[32] A. Yazdani and R. Iravani, *Voltage-Sourced Converters in Power Systems: Modeling, Control, and Applications*. Hoboken, NJ, USA: Wiley, 2010.
[33] J. Fang, H. Li, Y. Tang, and F. Blaabjerg, "Distributed power system virtual inertia implemented by grid-connected power converters," *IEEE Trans. Power Electron.*, vol. 33, no. 10, pp. 8488–8499, Oct. 2018, doi: 10.1109/TPEL.2017.2785218.
[34] A. Reznik, M. G. Simoes, A. Al-Durra, and S. M. Muyeen, "LCL filter design and performance analysis for small wind turbine systems," in *Proc. IEEE Power Electron. Mach. Wind Appl.*, Jul. 2012, pp. 1–7.
[35] S. A. Khajehoddin, M. Karimi-Ghartemani, P. K. Jain, and A. Bakhshai, "A control design approach for three-phase grid-connected renewable energy resources," *IEEE Trans. Sustain. Energy*, vol. 2, no. 4, pp. 423–432, Oct. 2011.
[36] M. Liserre, F. Blaabjerg, and S. Hansen, "Design and control of an LCL-filter-based three-phase active rectifier," *IEEE Trans. Ind. Appl.*, vol. 41, no. 5, pp. 1281–1291, Oct. 2005.
[37] B. Liu and B.-M. Song, "Modeling and analysis of an LCL filter for grid-connected inverters in wind power generation systems," in *Proc. IEEE Power Energy Soc. Gen. Meeting*, Jul. 2011, pp. 1–6.
[38] *IEEE Recommended Practices and Requirements for Harmonic Control in Electrical Power Systems*, Standard 519-2014, IEEE, 2014.
[39] K. H. Hussein, I. Muta, T. Hoshino, and M. Osakada, "Maximum photovoltaic power tracking: An algorithm for rapidly changing atmospheric conditions," *IEE Proc.-Generat., Transmiss. Distrib.*, vol. 142, no. 1, pp. 59–64, Jan. 1995.
[40] D. P. Hohm and M. E. Ropp, "Comparative study of maximum power point tracking algorithms using an experimental, programmable, maximum power point tracking test bed," in *Proc. Conf. Rec. 28th IEEE Photovoltaic Specialists Conf.*, 2000, pp. 1699–1702.
[41] *RTDS Simulator Help Manuals Documentation*. RTDS Technologies Inc. Winnipeg, MB, Canada. Accessed: Apr. 2021. [Online]. Available: https://www.rtds.com

AJINKYA J. SONAWANE (Graduate Student Member, IEEE) was born in Maharashtra, India. He received the B.E. degree in electrical engineering from Pune University, Maharashtra, in 2012, and the M.Tech. degree in integrated power system from YCCE, Nagpur, India, in 2015. He is currently pursuing the Ph.D. degree with the Department of Electrical Engineering, IIT Indore, Indore, India.

His current research interest includes renewable energy generation systems.

AMOD C. UMARIKAR (Member, IEEE) was born in Maharashtra, India. He received the M.Tech. degree in power electronics and power systems from the IIT Bombay, Mumbai, India, in 2000, and the Ph.D. degree in electrical engineering from the Indian Institute of Science, Bengaluru, India, in 2006.

He is currently an Associate Professor with the Department of Electrical Engineering, IIT Indore, Indore, India. His current research interests include the application of power electronics in renewable energy systems and power quality.